LETTER

Intrinsically stretchable and healable semiconducting polymer for organic transistors

Jin Young Oh[1]*, Simon Rondeau-Gagné[1]*†, Yu-Cheng Chiu[1]*†, Alex Chortos[1], Franziska Lissel[1], Ging-Ji Nathan Wang[1], Bob C. Schroeder[1]†, Tadanori Kurosawa[1], Jeffrey Lopez[1], Toru Katsumata[1,2], Jie Xu[1], Chenxin Zhu[3], Xiaodan Gu[1,4], Won-Gyu Bae[1], Yeongin Kim[3], Lihua Jin[5], Jong Won Chung[1,6], Jeffrey B.-H. Tok[1] & Zhenan Bao[1]

Thin-film field-effect transistors are essential elements of stretchable electronic devices for wearable electronics[1,2]. All of the materials and components of such transistors need to be stretchable and mechanically robust[3,4]. Although there has been recent progress towards stretchable conductors[5–8], the realization of stretchable semiconductors has focused mainly on strain-accommodating engineering of materials, or blending of nanofibres or nanowires into elastomers[9–11]. An alternative approach relies on using semiconductors that are intrinsically stretchable, so that they can be fabricated using standard processing methods[12]. Molecular stretchability can be enhanced when conjugated polymers, containing modified side-chains and segmented backbones, are infused with more flexible molecular building blocks[13,14]. Here we present a design concept for stretchable semiconducting polymers, which involves introducing chemical moieties to promote dynamic non-covalent crosslinking of the conjugated polymers. These non-covalent crosslinking moieties are able to undergo an energy dissipation mechanism through breakage of bonds when strain is applied, while retaining high charge transport abilities. As a result, our polymer is able to recover its high field-effect mobility performance (more than 1 square centimetre per volt per second) even after a hundred cycles at 100 per cent applied strain. Organic thin-film field-effect transistors fabricated from these materials exhibited mobility as high as 1.3 square centimetres per volt per second and a high on/off current ratio exceeding a million. The field-effect mobility remained as high as 1.12 square centimetres per volt per second at 100 per cent strain along the direction perpendicular to the strain. The field-effect mobility of damaged devices can be almost fully recovered after a solvent and thermal healing treatment. Finally, we successfully fabricated a skin-inspired stretchable organic transistor operating under deformations that might be expected in a wearable device.

Incorporation of dynamic non-covalent crosslinking between flexible polymer chains is an important method of achieving high stretchability and self-healing properties[15,16]. The dynamic bonds can easily be broken to allow energy dissipation upon strain, thus making the system more tolerant of strain and mechanical stimuli. Moreover, the bonds can be reformed to recover the initial mechanical property and self-heal. Among the different types of dynamic bonds, hydrogen bonds are particularly suitable for skin-inspired electronics owing to their spontaneous formation and healing ability[17–20]. Such polar substituents in organic semiconductors have received increased attention in recent organic electronics research, but mostly in producing self-assembled nanostructures instead of using them to improve mechanical properties[21].

2,6-pyridine dicarboxamide (PDCA) was chosen to introduce hydrogen bonding within the flexible polymer backbone since this unit contains two amide groups possessing moderate hydrogen-bonding strength, allowing the formation of a polymer network without drastically increasing the tensile modulus of the material[22,23]. Previous work has indicated that introducing a small fraction of non-conjugated units to the polymer backbone does not noticeably degrade the charge transport mobility[24]. Here we introduce alkyl spacers to enhance the flexibility of the dynamic moieties. Semiconducting polymers incorporating different ratios of non-conjugated PDCA moiety were thus synthesized (**P1** to **P4**; structures shown in Fig. 1a). To confirm the presence of hydrogen bonds, both X-ray crystallography and nuclear magnetic resonance (NMR) experiments (Extended Data Figs 1 and 2, and Supplementary Figs 1, 2 and 11) were used to ascertain hydrogen-bond formation in PDCA-containing model compounds.

Initial evaluation of the electrical properties was performed using organic thin-film field-effect transistor (OTFT) devices (Fig. 1b). For devices fabricated with **P2** and **P3**, the measured mobilities were both $>1\,cm^2\,V^{-1}\,s^{-1}$. Even with **P4** (containing 20 mol% of non-conjugated monomers), its field-effect mobility remained as high as $0.58\,cm^2\,V^{-1}\,s^{-1}$ (Supplementary Fig. 12). To understand further the contributions from the disruption of conjugation and incorporation of hydrogen bonding on the mechanical properties of the polymers, we next measured the elastic modulus of the polymers (Fig. 1c and Supplementary Fig. 13). All the polymers with PDCA moieties exhibited a lower elastic modulus than that of the fully conjugated polymer (**P1**). Although intermolecular hydrogen bonding essentially cross-links the polymers and thus should increase the elastic modulus of the polymer film[25], it appears that disruption of conjugation—that is, reducing the rigidity of the conjugated polymer backbone—has a larger effect on the elastic modulus of the polymer semiconductor film. We attributed the reduction in the measured elastic modulus to the changes in film morphology, such as the increase in the amorphous fraction in the polymer film or the decrease in relative crystallinity (Fig. 1e), and also a slight reduction of the average size of crystallites (Extended Data Fig. 3c), as characterized by grazing incidence X-ray diffraction analysis (Supplementary Fig. 14).

To gain further insight into the molecular level changes during stretching, the degree of polymer chain alignment under strain was measured using polarized ultraviolet–visible spectroscopy and quantified using dichroic ratios (Fig. 1d and Supplementary Fig. 16). The dichroic ratio of **P1** initially increased slightly with strain owing to strain-induced chain alignment, but soon decreased to approximately 1; this was caused by chain relaxation due to crack formation upon
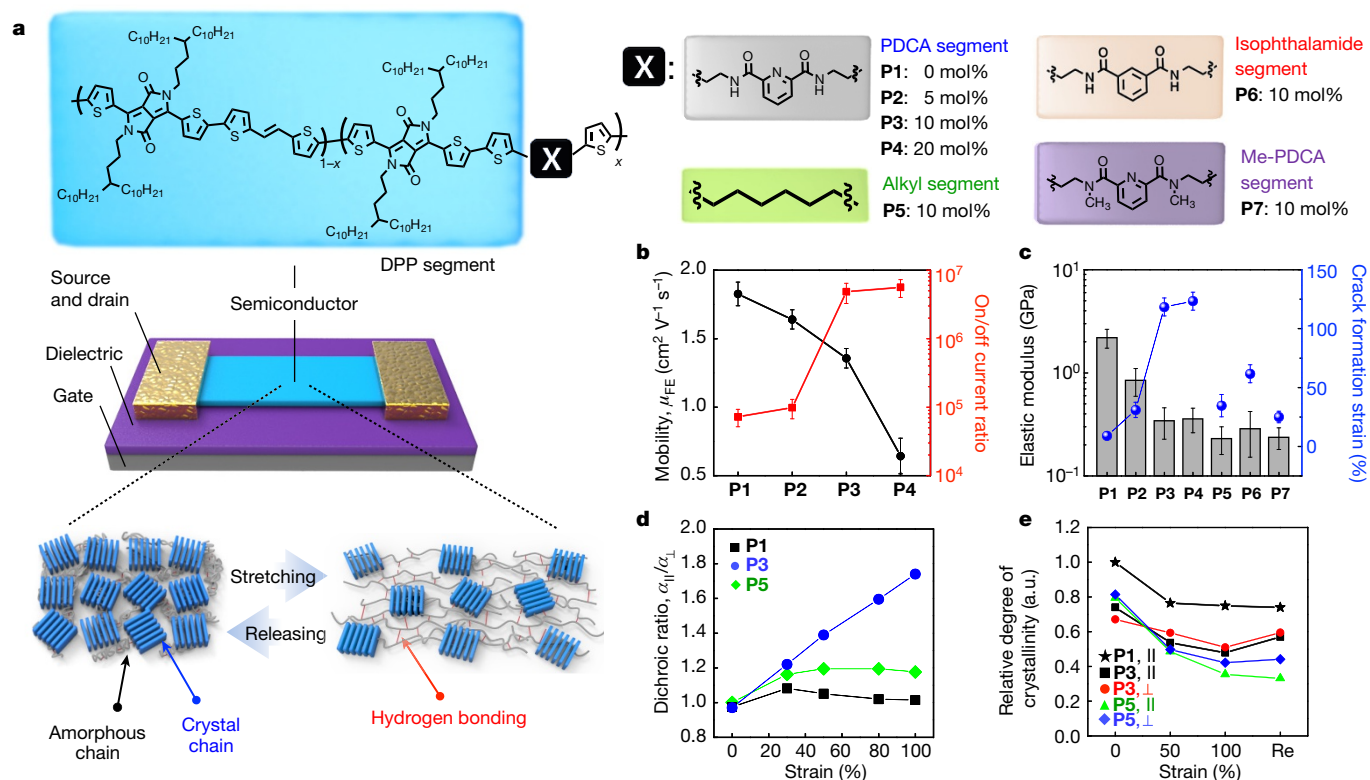
Figure 1 | Design of stretchable and healable semiconducting polymer OTFTs and their performance characterizations. a, Chemical structures of polymers **P1** to **P7** and general mechanism for enhancement of stretchability in conjugated polymers via dynamic bonding. The stretchable semiconducting polymers are based on 3,6-di(thiophen-2-yl)-2,5-dihydropyrrolo[3,4-c]pyrrole-1,4-dione (DPP) repeating units and non-conjugated 2,6-pyridine dicarboxamide (PDCA) moieties introduced directly in the polymer backbone as hydrogen bonding units. To qualitatively evaluate the stretching properties of the polymers, thin films are supported on polydimethylsiloxane (PDMS) substrates and stretched to different strain ratios (0% to 100% strain; 'Re' refers to the value after strain release). **b,** Field-effect mobility μ_{FE} and on/off current ratios of **P1** to **P4** as measured by conventional OTFTs (the source and drain electrodes are 40-nm-thick Au, the dielectric layer is 300-nm-thick SiO_2 and the gate

electrode is highly doped silicon substrate). **c,** Influence of the hydrogen-bonding moiety amount on elastic modulus and crack formation strain. Error bars in **b** (three batches of samples were prepared, and five OTFTs from each sample were measured) and **c** (one data point was obtained from each sample, and three batches of samples were prepared and measured) are mean ± s.d. **d,** Dichroic ratios of **P1**, **P3** and **P5** under various strain levels. $\alpha_\parallel$ and $\alpha_\perp$ are absorption intensities measured with the polarization direction of light parallel and perpendicular to the stretching direction, respectively. **e,** Influence of the strain ratio on the relative degree of crystallinity extracted from peak (200) for both 'parallel' and 'perpendicular' directions of **P1**, **P3** and **P5**. Owing to the formation of large cracks, the relative degree of crystallinity of **P1** perpendicular to the strain direction was not measured. The semiconductor is 35 nm thick. (a.u., arbitrary units.)

increasing the strain from 30% to 100%. This observation indicates that **P1** is not very stretchable and, indeed, we observed that cracks began to form even at low strains (5%–10%); these were further confirmed by both optical microscopy and atomic force microscopy (AFM). On the other hand, the dichroic ratio of **P3** increased linearly to 1.8, as strain increased from 30% to 100%. This observation is consistent with our microscopic observations that no microscale cracks were formed for **P3**, even with strain as high as 100%, showing that polymer chain alignment by strain can be achieved (Supplementary Figs 17 and 18 and Extended Data Fig. 3).

Relative degree of crystallinity analysis was used next to examine the change of morphology under strain (Fig. 1e and Supplementary Figs 19 and 20). The relative degree of crystallinity of **P1** decreased with strain from 0% to 50%, and plateaued from 50% onwards. This observation, combined with AFM studies, indicates that the tensile strain applied to the thin film was initially released through breakage of the crystalline regions until crack formation. In contrast, the relative degree of crystallinity of **P3** decreased steadily upon applied strain from 0% to 100%. Upon releasing the strain, we observed that the relative degree of crystallinity recovered only partially, indicating that some of its crystalline domains may be permanently altered or broken apart by the applied strain. This result, combined with the steady increase in dichroic ratio previously observed, suggests that **P3** has multiple mechanisms for energy dissipation during strain: (1) stretching and

realignment of polymer chains in amorphous regions; (2) breaking of some of the crystalline domains; and (3) breakage of hydrogen bonding.

The mechanism of energy dissipation through hydrogen-bond breakages has previously been observed[18]. We confirmed this benefit of incorporating hydrogen-bonding sites as strain-releasing moieties by comparison with several reference polymers. **P5** contains 10 mol% of non-conjugated alkyl spacers, that is, no PDCA moieties, on its polymer backbone (Fig. 1a). Despite having a lower elastic modulus than **P3**, **P5** can achieve a maximum strain of only 30% before cracks form, a value much lower than that of **P3**'s maximum strain (110%). Furthermore, the measured maximum dichroic ratio for **P5** was found to be only about 1.16 at 30% strain, consistent with the strain value at the onset of crack formation. In addition, the relative crystallinity of **P5** was measured to be lower than **P1**, indicating that an increase in the fraction of amorphous regions has occurred within the polymer thin film, similar to **P2–P4**.

However, when 100% strain was applied to the film, the relative degree of crystallinity decreased drastically from 0.80 to 0.35, indicating that the tensile energy in **P5** film is dissipated primarily through the breaking of crystallites (Supplementary Fig. 21). This observation is consistent with a recent report, which did not show much improvement on fracture strain with conjugation breakage of another DPP polymer[24]. **P6** is another reference polymer, in which the pyridine moiety was replaced by a benzene ring while the amide moieties remain (Fig. 1a).
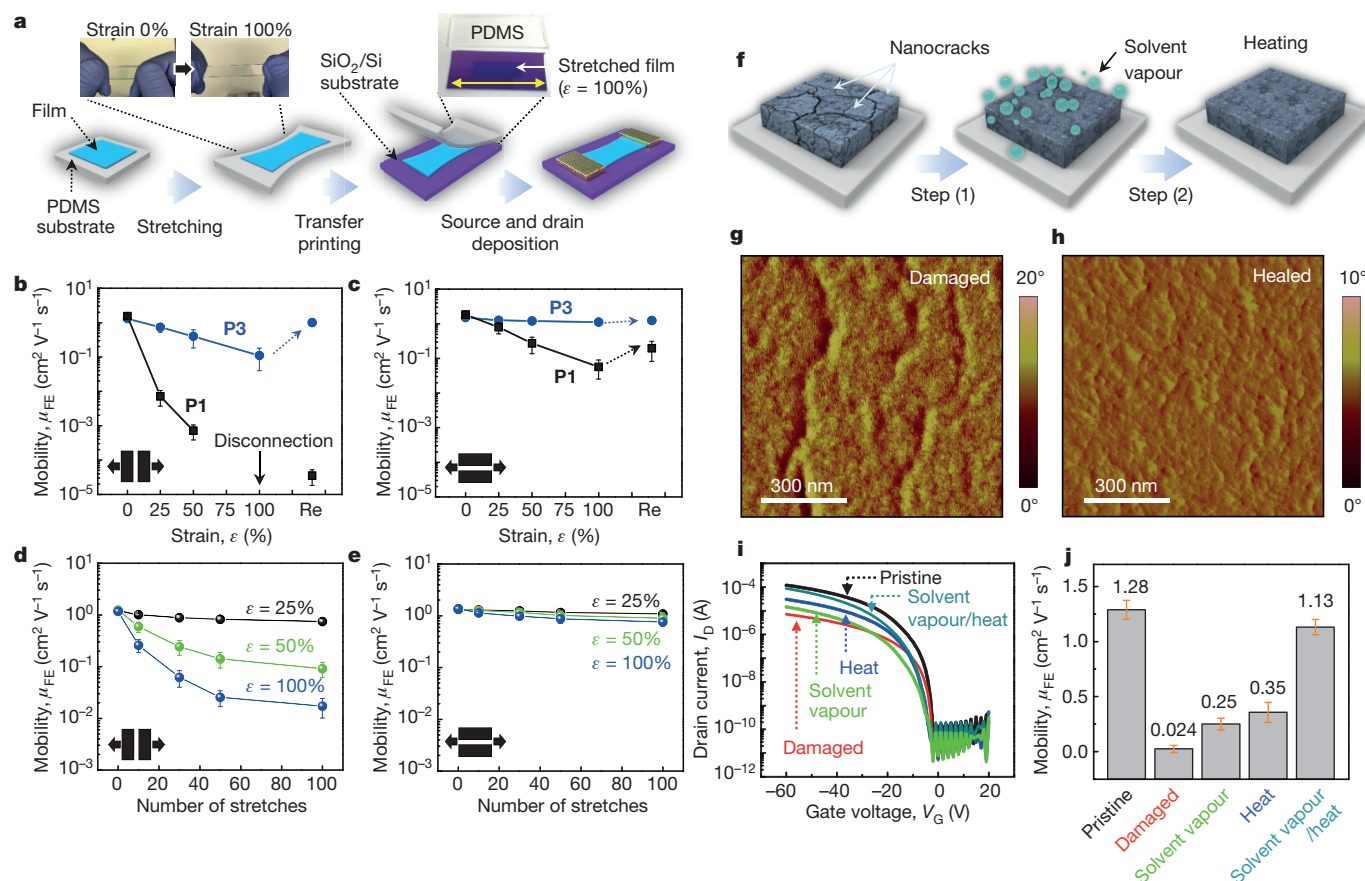
Figure 2 | Charge transport of semiconducting polymers under applied strain and their healing properties. a, Fabrication process for OTFTs with stretched polymer thin films. **b, c**, Field-effect mobility μ_{FE} as a function of various strains along the strain direction (**b**) and perpendicular to strain direction (**c**). **d, e**, Field-effect mobility versus number of stretching cycles performed along the strain direction (**d**) and perpendicular to strain direction (**e**). **f**, Representation of the treatments used for healing the conjugated polymer films. **g, h**, AFM phase image for damaged (**g**) and healed (**h**) film of **P3**. **i, j**, Transfer curves (**i**) and field-effect mobility (**j**) of damaged and healed **P3** OTFTs. Error bars in **b, c, d, e** and **j** are mean ± s.d. (three batches of samples were prepared, and three OTFTs from each sample were measured).
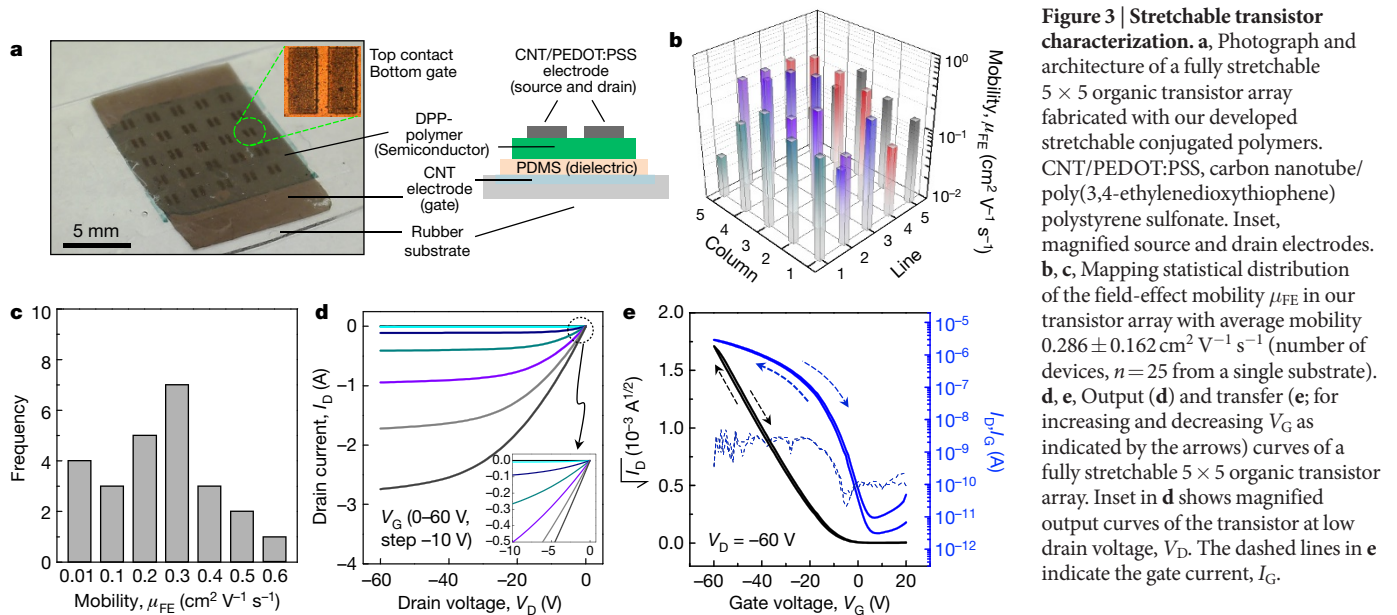
P6 was observed to possess enhanced stretchability compared to polymers **P1** and **P5** (Fig. 1c and Supplementary Fig. 18f), which again suggests the importance of the intermolecular hydrogen bonding for enhanced mechanical properties. However, as compared to polymers **P2**, **P3** and **P4** (all containing pyridine moieties), its stretchability was reduced. This suggests that the introduction of pyridine moieties may contribute to the enhanced mechanical properties either through participating in intra- and intermolecular hydrogen-bonding or through changing the morphology of the film. Finally, reference polymer **P7** was synthesized to remove the hydrogen-bonding amide hydrogens (Fig. 1a). **P7** showed a decreased stretchability with an onset strain for crack formation of about 25% (Fig. 1c and Supplementary Fig. 18g). The above control experiments with reference polymers further confirm the important contribution of the dynamic non-covalent hydrogen-bond-forming moieties as strain-releasing elements for enhancing the stretchability of conjugated polymers.

To evaluate the charge transport behaviour of our fabricated stretchable semiconducting polymers, OTFTs were fabricated and characterized (Fig. 2a). On applying strains up to 100%, we observed that the average field-effect mobility of the **P3** device decreased moderately, from $1.32\,cm^2\,V^{-1}\,s^{-1}$ to $0.11\,cm^2\,V^{-1}\,s^{-1}$, along the direction of applied strain. Furthermore, the mobility was observed to recover to $1.00\,cm^2\,V^{-1}\,s^{-1}$ upon releasing the applied strain. When the strain is applied in a perpendicular direction, the mobility of the **P3** device is maintained, that is, $>1\,cm^2\,V^{-1}\,s^{-1}$, up to 100% strain and even after release. In contrast, the mobility of the **P1** device degraded substantially even at 25% applied strain, and was totally non-functional at 100% strain. Unlike **P3**, the mobility of the **P1** device is unable to recover upon stress release.

Besides a single stretching event, we also performed rigorous repeated stretching cycle tests on the **P3** devices at various strains (Fig. 2d, e). After stretching the device for 100 cycles between 0% and 25% strain, the mobility along the stretching direction was decreased by about 40% (that is, from $1.2\,cm^2\,V^{-1}\,s^{-1}$ to $0.74\,cm^2\,V^{-1}\,s^{-1}$) and was further reduced to $0.017\,cm^2\,V^{-1}\,s^{-1}$ when subjected to 100% strain. However, when the strain was along the perpendicular direction, the device showed higher durability and robustness. Even after 100 cycles up to 100% strain, only a 26% decrease in mobility was observed. Only a 19% decrease in mobility was observed for 100 cycles up to 25% strain (Supplementary Fig. 22).

In addition to intrinsic stretchability, the healing ability enabled by the dynamic bonding represents another major advantage of the polymer design. Although the self-healing abilities of non-conjugated polymer networks cross-linked with hydrogen-bonding sites have been reported[26], self-healing ability has not been investigated for conjugated polymers. To facilitate efficient healing for damaged **P3** films, post treatments via heat and solvent annealing are required to promote polymer chain movement (Fig. 2f). When applied independently, both thermal and solvent annealing greatly reduced the size and density of the nanocracks. However, the field-effect mobility was observed to be only slightly recovered (Fig. 2g–j and Supplementary Fig. 23).

Solvent annealing applied in conjunction with thermal annealing promoted the most efficient healing of the polymer films. Specifically, we observed a complete disappearance of the nanocracks within the damaged films, and more importantly, an almost complete recovery of the average field-effect mobility to $1.13\,cm^2\,V^{-1}\,s^{-1}$ (Fig. 2i, j and Supplementary Fig. 23). Additionally, the dependence of dichroic ratio

Figure 3 | Stretchable transistor characterization. a, Photograph and architecture of a fully stretchable 5×5 organic transistor array fabricated with our developed stretchable conjugated polymers. CNT/PEDOT:PSS, carbon nanotube/ poly(3,4-ethylenedioxythiophene) polystyrene sulfonate. Inset, magnified source and drain electrodes. **b**, **c**, Mapping statistical distribution of the field-effect mobility μ_{FE} in our transistor array with average mobility $0.286 \pm 0.162 \, cm^2 \, V^{-1} \, s^{-1}$ (number of devices, $n = 25$ from a single substrate). **d**, **e**, Output (**d**) and transfer (**e**; for increasing and decreasing V_G as indicated by the arrows) curves of a fully stretchable 5×5 organic transistor array. Inset in **d** shows magnified output curves of the transistor at low drain voltage, V_D. The dashed lines in **e** indicate the gate current, I_G.

on strain completely recovered to a level similar to that of a pristine undamaged film, indicating the healed film has most probably returned to its original film morphology. In comparison, our various applied healing conditions did not improve the damaged **P1** and **P5** films (Supplementary Figs 24–28 and Extended Data Fig. 4). To the best

of our knowledge, this is the first demonstration of complete healing (albeit non-autonomous) of a high field-effect mobility conjugated polymer after mechanical damages.

Equipped with our newly developed high mobility and high stretchability polymer semiconductor, we proceed to fabricate fully stretchable
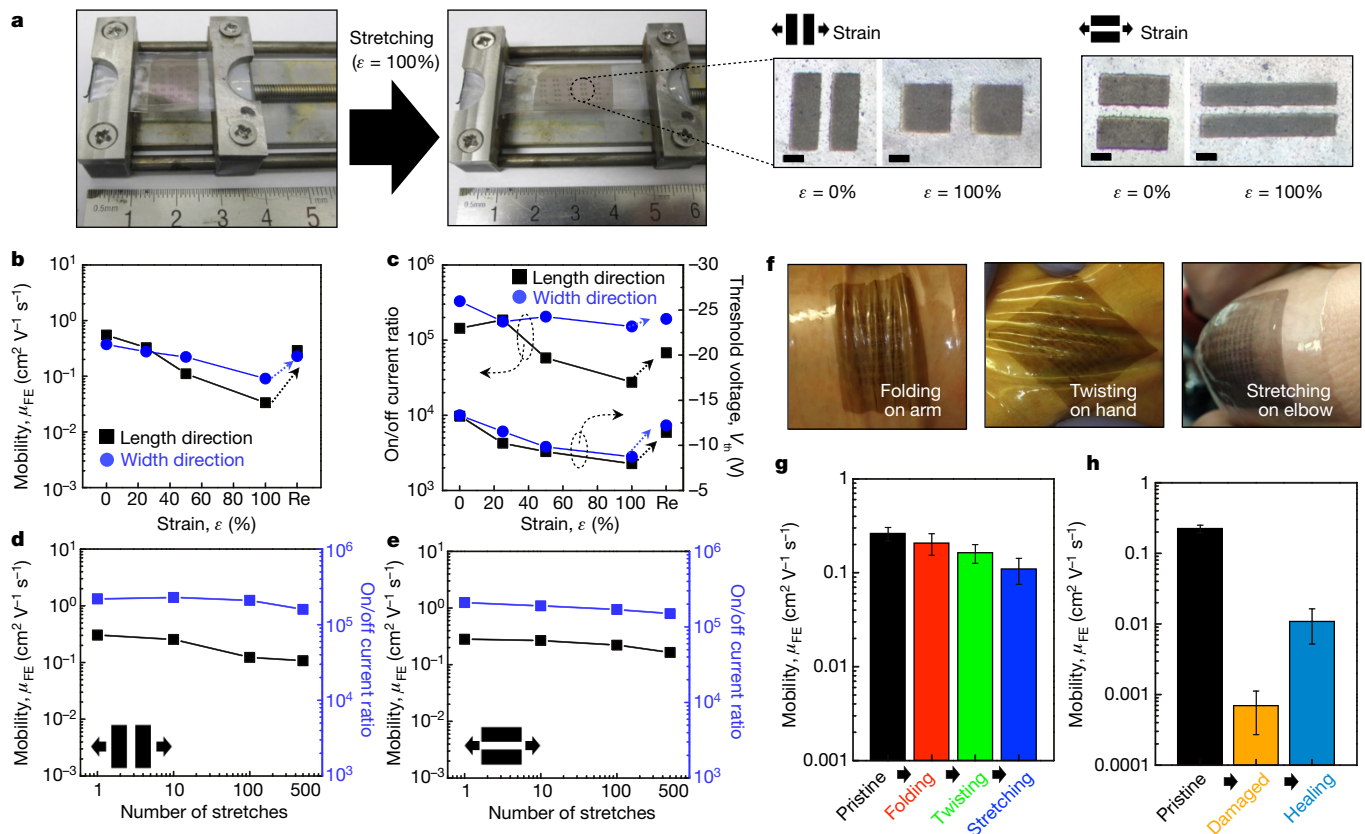

Figure 4 | Stretchable transistor as skin-inspired wearable device. a, *In situ* stretching images of stretchable OTFT from 0% to 100% strain (scale bars in close-ups, $300 \, \mu m$). **b**, **c**, Field-effect mobility μ_{FE} (**b**) and on/off current ratio and threshold voltage V_{th} (**c**) of a stretchable transistor during a stretching cycle. **d**, **e**, Mobility and on/off ratio of OTFTs for 500 stretching cycles at 25% strain along channel length and width directions,

respectively. **f**, Photographs of folded, twisted and stretched OTFTs on human skin. **g**, OTFT mobilities after various extreme human motions. **h**, Mobilities of mechanically damaged OTFTs before and after healing process. Error bars in **g** and **h** are mean ± s.d. (five batches of samples were prepared, and one OTFT from each sample was measured).

OTFTs (5×5 arrays; Fig. 3a, Supplementary Fig. 29 and Extended Data Fig. 5). Our obtained device yield is 100%, along with good switching performance (Fig. 3b–e). Furthermore, most of the devices exhibited field-effect mobilities in the range of about $10^{-1} \mathrm{cm^2\,V^{-1}\,s^{-1}}$ with $>10^5$ on/off current ratio (Supplementary Fig. 29). In specific, the highest value obtained for the mobility is $0.6\,\mathrm{cm^2\,V^{-1}\,s^{-1}}$, while the average mobility was $0.28\,\mathrm{cm^2\,V^{-1}\,s^{-1}}$. In general, we observed that the fully stretchable OTFTs all exhibited lower mobilities compared to OTFTs as fabricated on rigid Si/SiO$_2$ substrates treated with self-assembled monolayer of n-octadecyltrimethoxysilan (OTS). We attributed this observation to the lower applied electric field with a thicker layer of dielectric on the stretchable OTFTs devices (Supplementary Fig. 30). The stretchable devices showed little hysteresis and low gate-leakage currents. These measured performance parameters represent the best of the current reported stretchable organic semiconductors and fully stretchable OTFTs (Supplementary Tables 3 and 4)[27–30].

To verify the stretchability of our organic transistors, we investigated their electrical performance by subjecting them to various strenuous mechanical strain conditions. The transistors showed a slow linear decrease in mobility when being strained up to 100%. After releasing the strain, the mobility was observed to recover to close to its initial values (Fig. 4b and Supplementary Fig. 31). The same trend was also observed for the on/off current ratios. These trends are qualitatively similar to the trend observed when only the polymer semiconductor is stretched. Most practical applications, however, require effective operation only for applied strains of 20% to 30%, so we performed stretching durability tests at 25% strain and 500 cycles for our fabricated stretchable transistors (Fig. 4d, e). We observed that both the field-effect mobility and on/off current ratio of our transistors did not suffer any noticeable decrease in performance. Furthermore, we mounted our fabricated devices on human limbs to test device tolerance to various common movements, such as folding of the arm, twisting of the hand, and stretching of the elbow. Our device is able to maintain its average mobility at $>0.1\,\mathrm{cm^2\,V^{-1}\,s^{-1}}$ (Supplementary Fig. 32) under all these conditions. Finally, the healing ability of the polymer semiconductor can again be observed using the heating and solvent annealing process we developed (Fig. 4h and Supplementary Fig. 33).

Online Content Methods, along with any additional Extended Data display items and Source Data, are available in the online version of the paper; references unique to these sections appear only in the online paper.

1. Chortos, A. & Bao, Z. Skin-inspired electronic devices. *Mater. Today* **17,** 321–331 (2014).
2. Wagner, S. & Bauer, S. Materials for stretchable electronics. *MRS Bull.* **37,** 207–213 (2012).
3. Savagatrup, S. *et al.* Molecularly stretchable electronics. *Chem. Mater.* **26,** 3028–3041 (2014).
4. Hammock, M. L. *et al.* 25th anniversary article: the evolution of electronic skin (e-skin): a brief history, design, consideration, and recent progress. *Adv. Mater.* **25,** 5997–6038 (2013).
5. Yao, S. & Zhu, Y. Nanomaterial-enabled stretchable conductors: strategies, materials, and devices. *Adv. Mater.* **27,** 1480–1511 (2015).
6. Benight, S. J., Wang, C., Tok, J. B. H. & Bao, Z. Stretchable and self-healing polymers and devices for electronic skin. *Prog. Polym. Sci.* **38,** 1961–1977 (2013).
7. Oh, J. Y. *et al.* Conducting polymer dough for deformable electronics. *Adv. Mater.* **28,** 4455–4461 (2016).
8. Sekitani, T. *et al.* Stretchable active-matrix organic light-emitting diode display using printable elastic conductors. *Nat. Mater.* **8,** 494–499 (2009).
9. Kaltenbrunner, M. *et al.* Ultrathin and lightweight organic solar cells with high flexibility. *Nat. Commun.* **3,** 770 (2012).
10. Khang, D.-Y., Jiang, H., Huang, Y. & Rogers, J. A. A stretchable form of single-crystal silicon for high performance electronics on rubber substrates. *Science* **311,** 208–212 (2006).
11. Shin, M. *et al.* Polythiophene nanofibril bundles surface-embedded in elastomer: a route to a highly stretchable active channel layer. *Adv. Mater.* **27,** 1255–1261 (2015).
12. O'Connor, B. *et al.* Anisotropic structure and charge transport in highly strain-aligned regioregular poly(3-hexylthiophene). *Adv. Funct. Mater.* **21,** 3697–3705 (2011).
13. Müller, C. *et al.* Tough, semiconducting polyethylene-poly(3-hexylthiophene) diblock copolymers. *Adv. Funct. Mater.* **17,** 2674–2679 (2007).
14. Printz, A. D. *et al.* Increased elasticity of a low-bandgap conjugated copolymer by random segmentation for mechanically robust solar cells. *RSC Adv.* **4,** 13635–13643 (2014).
15. Yang, Y. & Urban, M. W. Self-healing polymeric materials. *Chem. Soc. Rev.* **42,** 7446–7467 (2013).
16. Black Ramirez, A. L. *et al.* Mechanochemical strengthening of a synthetic polymer in response to typically destructive shear forces. *Nat. Chem.* **5,** 757–761 (2013).
17. Chen, Y., Kushner, A. M., Williams, G. A. & Guan, Z. Multiphase design of autonomic self-healing thermoplastic elastomers. *Nat. Chem.* **4,** 467–472 (2012).
18. Sun, J. Y. *et al.* Highly stretchable and tough hydrogels. *Nature* **489,** 133–136 (2012).
19. Cordier, P., Tournilhac, F., Soulié-Ziakovic, C. & Leibler, L. Self-healing and thermoreversible rubber from supramolecular assembly. *Nature* **451,** 977–980 (2008).
20. Yuk, H. *et al.* Tough bonding of hydrogels to diverse non-porous surfaces. *Nat. Mater.* **15,** 190–196 (2015).
21. Gsänger, M. *et al.* Organic semiconductors based on dyes and color pigments. *Adv. Mater.* **28,** 3615–3645 (2016).
22. Ray, M., Ghosh, D., Shirin, Z. & Mukherjee, R. Highly stabilized low-spin iron(III) and cobalt(III) complexes of a tridentate bis-amide ligand 2,6-bis (N-phenylcarbamoyl)pyridine. Novel nonmacrocyclic tetraamido-N coordination and two unusually short metal-pyridine bonds. *Inorg. Chem.* **36,** 3568–3572 (1997).
23. Marlin, D. S., Olmstead, M. M. & Mascharak, P. K. Extended structures controlled by intramolecular and intermolecular hydrogen bonding: a case study with pyridine-2,6-dicarboxamide, 1,3-benzenedicarboxamide and N, N′-dimethyl-2,6-pyridinedicarboxamide. *J. Mol. Struct.* **554,** 211–223 (2000).
24. Savagatrup, S. *et al.* Effect of broken conjugation on the stretchability of semiconducting polymers. *Macromol. Rapid Commun.* **37,** 1623–1628 (2016).
25. Langley, N. R. & Polmante, K. Relation of elastic modulus to crosslink and entanglement concentrations in rubber networks. *J. Polym. Sci. B* **12,** 1023–1034 (1974).
26. Herbst, F., Döhler, D., Michael, P. & Binder, W. H. Self-healing polymers via supramolecular forces. *Macromol. Rapid Commun.* **34,** 203–220 (2013).
27. Song, E. *et al.* Stretchable and transparent organic semiconducting thin film with conjugated polymer nanowires embedded in an elastomeric matrix. *Adv. Electron. Mater.* **2,** 1500250 (2016).
28. Wu, H.-C. *et al.* A rapid and facile soft contact lamination method: evaluation of polymer semiconductors for stretchable transistors. *Chem. Mater.* **26,** 4544–4551 (2014).
29. Chortos, A. *et al.* Highly stretchable transistor using microcracked organic semiconductor. *Adv. Mater.* **26,** 4253–4259 (2014).
30. Kaltenbrunner, M. *et al.* An ultra-lightweight design for imperceptible plastic electronics. *Nature* **499,** 458–463 (2013).

Supplementary Information is available in the online version of the paper.

Author Contributions J.Y.O., S.R.-G., Y.-C.C. and Z.B. conceived and designed the experiments. S.R.-G. and Z.B. designed the monomers and polymers. S.R.-G., B.C.S., T. Kurosawa, T. Katsumata and F.L. synthesized and characterized the monomers and polymers. J.Y.O. designed the device experiments and evaluated the stretchability of materials and devices. Y.-C.C. and J.Y.O. fabricated and optimized the OTFTs on solid substrates. J.Y.O. fabricated the fully stretchable OTFTs. J.Y.O., A.C., and C.Z. optimized the fully stretchable devices. J.Y.O. designed and performed the healing experiments. J.Y.O., G.-J.N.W., J.X., L.J., J.L., J.W.C., J.L. and Y.K. analysed the optical and mechanical properties of the polymer film. Y.-C.C. performed the grazing incidence X-ray diffraction experiments and analysis. Y.-C.C., X.G., J.Y.O. and Z.B. proposed the new mechanism concept. J.Y.O. and W.-G.B. designed and drew the three-dimensional computer graphics. J.Y.O., S.R.-G., Y.-C.C., J.B.-H.T. and Z.B. co-wrote the paper. All authors discussed the results and commented on the manuscript.

Author Information Reprints and permissions information is available at www.nature.com/reprints. The authors declare no competing financial interests. Readers are welcome to comment on the online version of the paper. Correspondence and requests for materials should be addressed to Z.B. (zbao@stanford.edu).

METHODS

All details of materials synthesis and structural characterizations can be found in the Supplementary Information.

Materials synthesis and characterization. Synthesis of DPP-based conjugated polymers containing non-conjugated PDCA units in the backbone was carried out via Stille polymerization using different ratios of PDCA-containing monomers (see Supplementary Information). Branched alkyl chains were installed on the DPP monomer in order to increase solubility and π–π stacking. We also selected (E)-2-(2-(thiophenyl-2-yl)vinyl)thiophene (TVT) as co-monomer. The non-conjugated monomer was reacted with the brominated DPP monomer and the distannylated TVT under Stille polymerization conditions to afford **P1** to **P4**. Polymers were purified by precipitation in methanol followed by Soxhlet extraction using methanol, acetone, hexanes and chloroform. All polymers showed good solubility in different solvents such as chloroform and chlorobenzene. Increasing the non-conjugated moiety content within the backbone also improved the solubility in polar solvents such as THF and DMF. The synthetic procedures for precursors, monomers and polymers are detailed in the Supplementary Information. Molecular weight, polydispersity index, monomers and polymer characterization are all detailed in the Supplementary Information. All results are from polymers with number average molecular weight M_n over 14 kDa and with a polydispersity below 4. Polymers with low M_n values showed less improvement in stretchability.

Thin-film characterization. To be consistent with films used for transistor fabrication and characterization, all films tested have thicknesses in the range 30–35 nm. They were spin-coated on OTS-treated SiO_2/Si substrate from chlorobenzene solution (5 mg ml^{-1}) at 2,000 r.p.m. in glove box and thermally annealed at 150 °C for 10 min. They were subsequently transferred to PDMS elastic substrates. The thin-film annealing temperature was found to affect stretchability. Significantly less improvement was observed for samples annealed at 150 °C for 30 min. Therefore, annealing for 10 min was used for all films. The morphology of polymer films was measured by optical microscopy and AFM. The molecular stretchability of polymer film was investigated by polarized ultraviolet–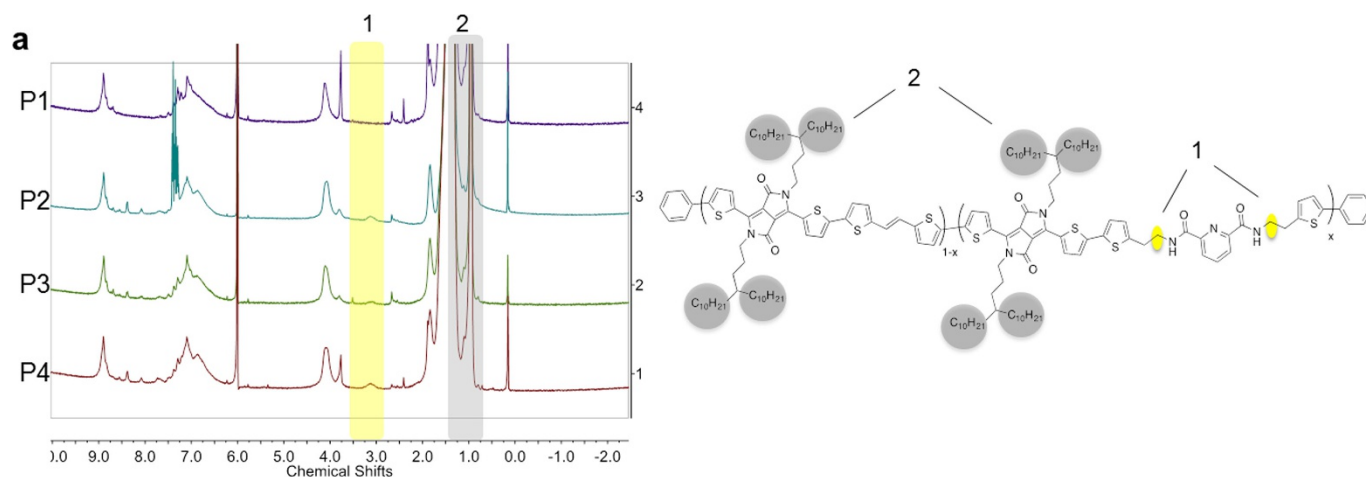visible spectroscopy. The elastic modulus of thin-films was measured using the buckling method (Supplementary Fig. 24). Grazing incidence X-ray diffraction was conducted at beamline 11-3 of the Stanford Synchrotron Radiation Lightsource. The incidence angle was 0.12 and the X-ray wavelength was 0.9758 Å, corresponding to a beam energy of 12.7 keV. All grazing incidence X-ray diffraction images were collected in reflection mode with a two-dimensional area detector and the sample under a helium atmosphere. Stretching and relaxing rates of the polymer thin films were performed at 0.65 mm s^{-1} (strain rate 2.6% s^{-1}).

Conventional organic transistors. The semiconducting polymer layer (35 nm) was spin-coated on OTS-treated SiO_2/Si substrate in glove box and was thermally annealed at 150 °C for 10 min. The source and drain electrodes (Au, 40 nm) were thermally evaporated under 5.0×10^6 Torr.

Skin-inspired organic transistor. Carbon nanotube (100 nm) film as the gate electronic was transferred onto polystyrene-block-poly(ethylene-ran-butylene)-block-polystyrene (SEBS) elastomer. The PDMS layer (1.8 μm) was then transferred onto a carbon nanotube/SEBS substrate. Then the semiconducting polymer layer (35 nm) was transferred on the PDMS dielectric layer. Finally, the PEDOT:PSS (30 nm)/carbon nanotube (70 nm) bilayer as the source and drain electrode was spray-coated onto the semiconducting layer. The transferring method for the device fabrication is depicted in Extended Data Fig. 5.

Healing process. For the solvent vapour treatment, the damaged sample is exposed to CHCl$_3$ vapour in a closed jar for 10 min at 40 °C. For the heat treatment, the sample is thermally annealed on a 150 °C hotplate for 30 min. For the combined solvent vapour and heat treatment, the sample first undergoes CHCl$_3$ vapour annealing (10 min at 40 °C) and then thermal annealing (30 min on hotplate at 150 °C).

31. Cellman, S. H., Dado, G. P., Liang, C.-B. & Adam, B. R. Conformation-directing effects of a single intramolecular amide–amide hydrogen bond: variable-temperature NMR and IR studies on a homologous diamide series. *J. Am. Chem. Soc.* **113,** 1164–1173 (1991).
32. Martin, R. B. Comparisons of indefinite self-association models. *Chem. Rev.* **96,** 3043–3064 (1996).
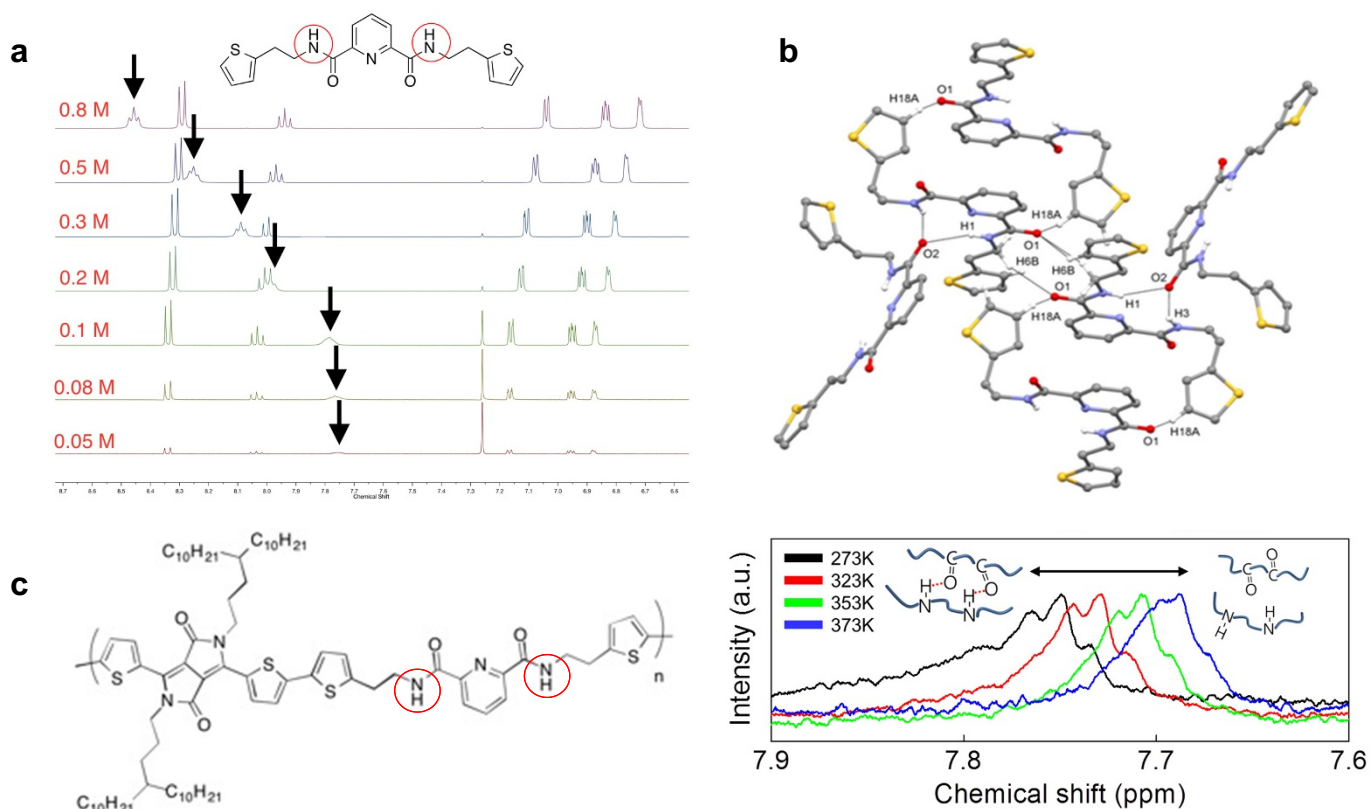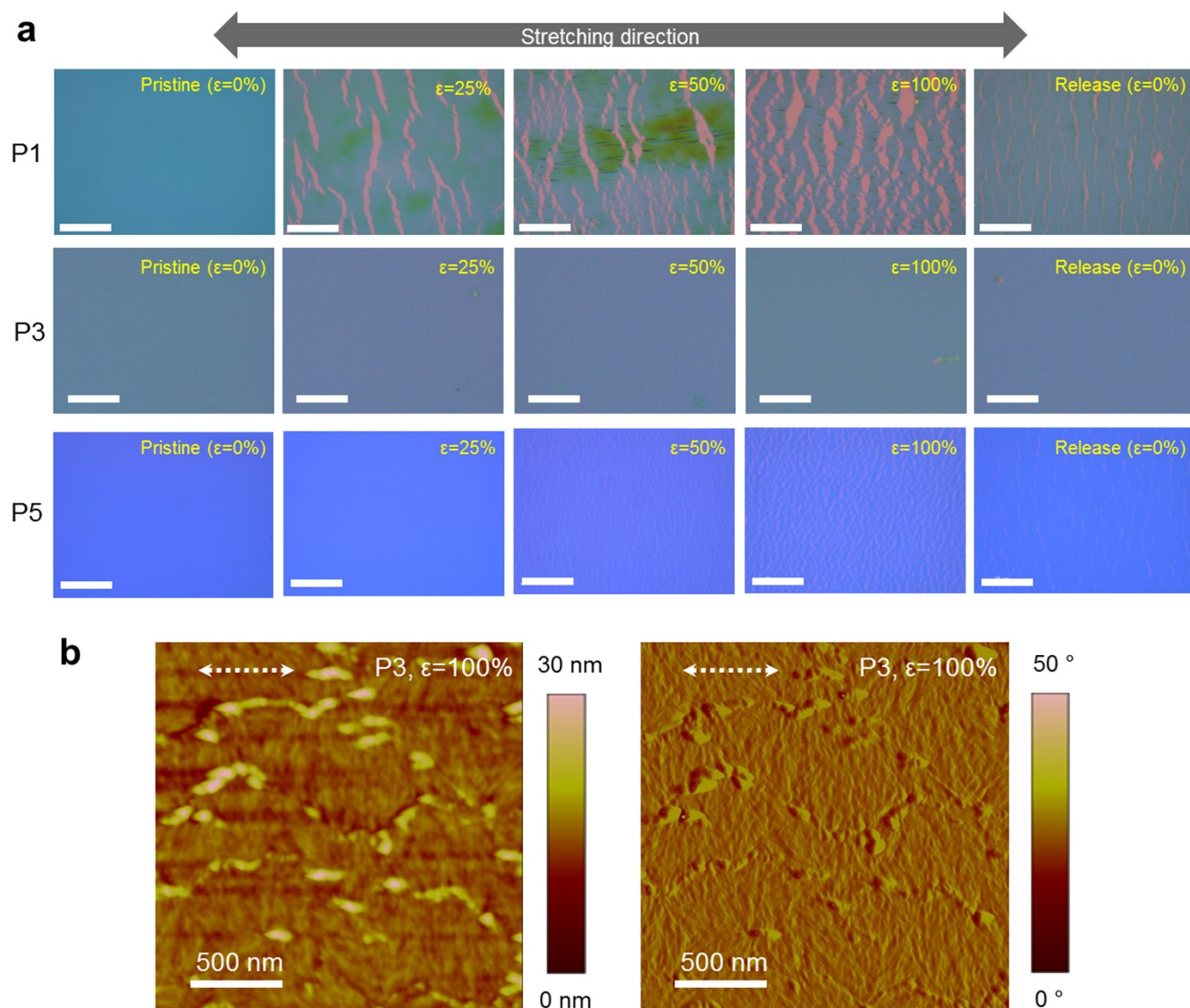
Extended Data Figure 1 | General characterization of P1–P4. a, Polymer composition by ^{1}H NMR. The ratio of PDCA moieties incorporated in the polymer backbone is determined by the integration of protons (**1**) versus the alkyl-chain terminal protons (**2**). **b,** General characterization of **P1–P4**. [a]Determined from thermogravimetric analysis. [b]The HOMO (highest occupied molecular orbital) energy level was calculated from cyclic voltammetry. Potentials versus Ag/AgCl using 0.1 M TBAPF$_6$ (tetrabutylammonium hexafluorophosphate) in CH$_3$CN (acetonitrile) as the electrolyte solution. [c]Calculated using the following equation: gap $= 1{,}240/\lambda_{onset}$ of polymer film. (PDI, polydispersity; T$_d$, degradation temperature; M$_w$, weight average molecular weight; λ, absorption wavelength in ultraviolet/visible spectroscopy).

	Theoretical ratio (1:2)	Calculated ratio (1:2)	M$_n$ (kDa)	M$_w$ (kDa)	PDI	T$_d$[a]	λ_{max} Sol,(nm)	λ_{max} Film,(nm)	HOMO[b] (eV)	Bandgap[c] (eV)
P1	0.00	0.00	20.4	65.4	3.2	>350	803, 738	801, 740	5.17	1.35
P2	0.05	0.06	19.7	61.4	3.3	>350	803, 738	801, 739	5.22	1.35
P3	0.10	0.09	16.2	49.1	3.0	>350	803, 738	801, 738	5.23	1.35
P4	0.20	0.17	13.4	35.5	2.6	>350	803, 738	801, 734	5.17	1.37

a

b

c

Extended Data Figure 2 | Intermolecular interactions between PDCA moieties. a, Chemical structure of model compound **1** and ^{1}H NMR at various concentrations of compound **1** in CDCl$_3$. Upon increasing concentration from 0.05 M to 0.8 M, a distinct shift of the amide proton (black arrow) towards low fields is observed. This indicates hydrogen bonding between the PDCA moieties, as previously observed[31]. A dimerization constant of 0.18 M^{-1} was determined by plotting concentration versus chemical shift and fitting using a dimer association model[32]. **b**, Molecular structure of **1** showing intermolecular hydrogen bonds determined by single-crystal X-ray diffraction. Ellipsoids are set

at the 30% probability level. Selected hydrogen atoms are omitted for clarity. **c**, Chemical structure of model oligomer **M1** and ^{1}H NMR of **M1** at various temperatures in 1,1,2,2-tetrachloroethane-d_2 showing the amide NH protons peak. The chemical shift upon temperature increase indicates a breaking of the hydrogen bonds formed between the polymer chains (shown as insets). Oligomer **M1** was used for this study because the solubility of the polymer was not sufficiently high to perform a similar study under high concentrations. (a.u., arbitrary units; ppm, parts per million.)
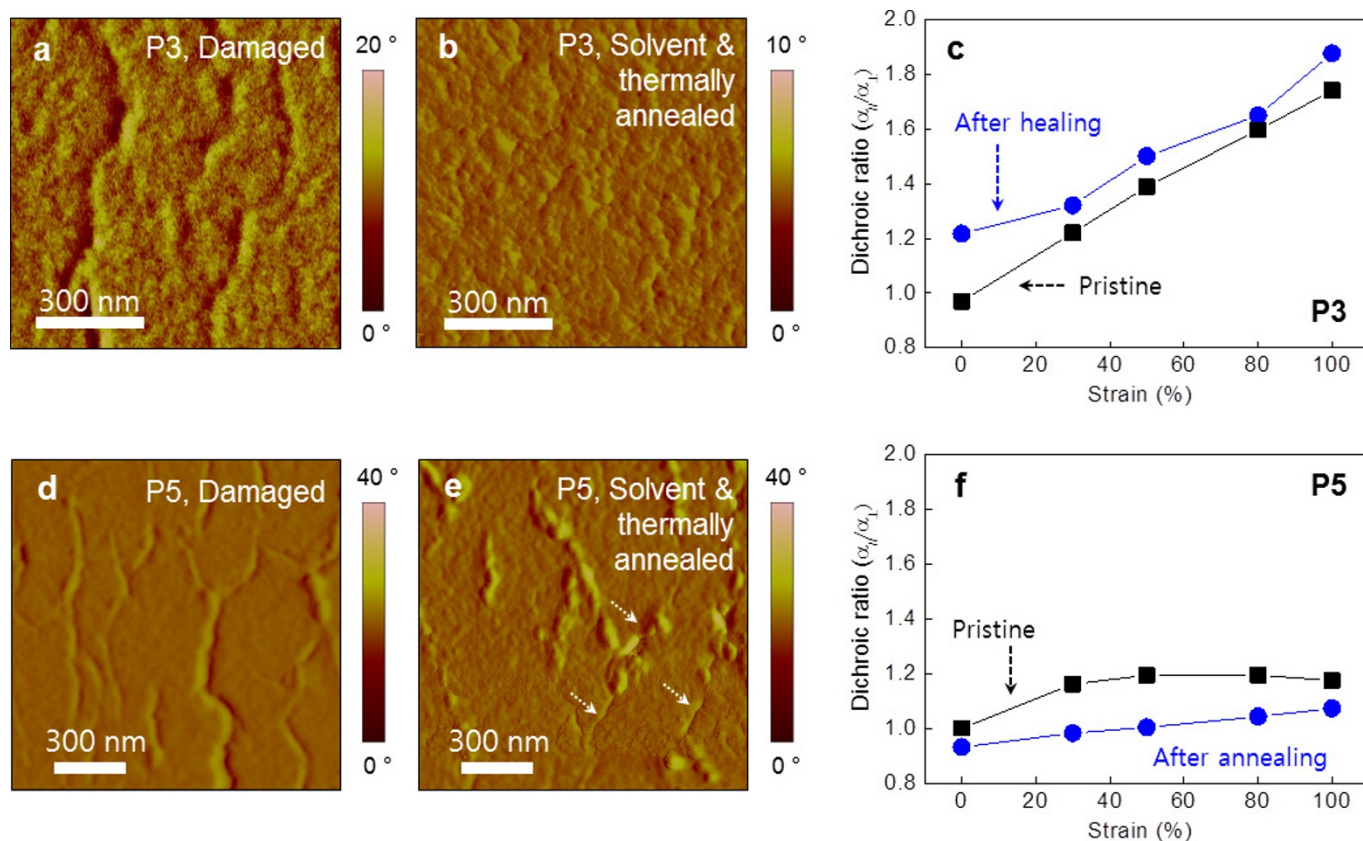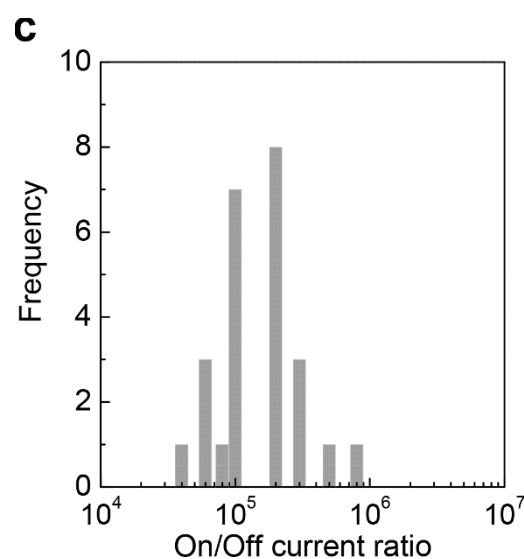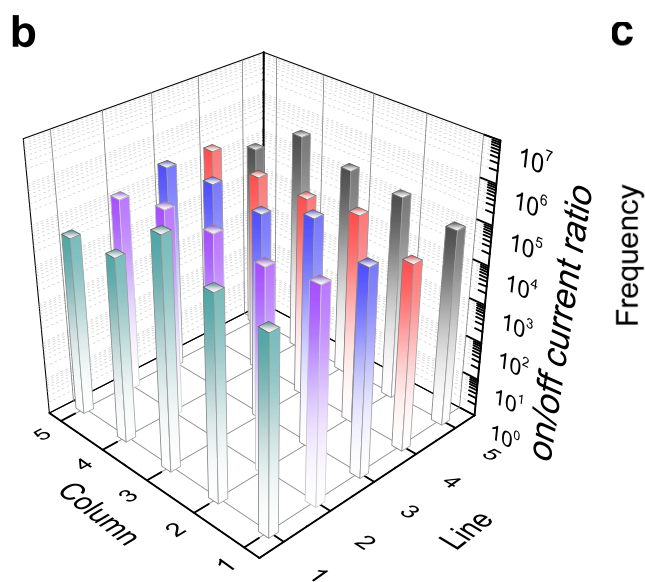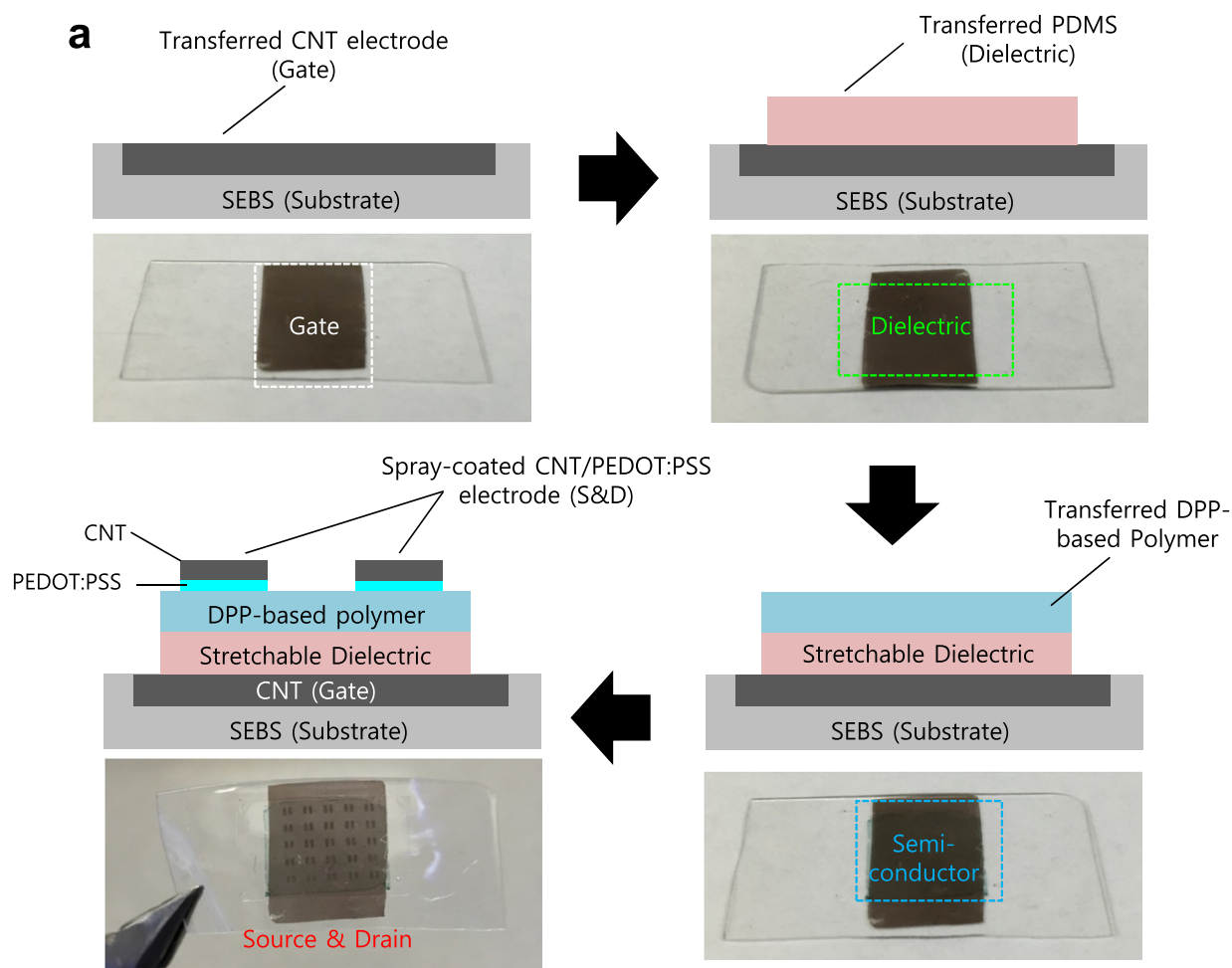
Extended Data Figure 3 | Behaviour of polymer thin-film under strain. **a**, Optical microscope images of **P1**, **P3** and **P5** as function of applied strain (0%–100%). **b**, Height and phase AFM images of **P3** under 100% strain showing no crack formation. **c**, Table of grazing incidence X-ray diffraction data for **P1** and **P3** films as a function of strain (0%–100%). The samples are annealed at 150 °C for 10 min. A reduction in the mean size of crystallites is observed for **P1** to **P3**. The semiconductor is 35 nm thick. (FWHM, full-width at half-maximum.)

Polymer	Applied Strain	FWHM at (200) peak \<parallel\>	Mean size of crystallites (nm)	FWHM at (200) peak \<perpendicular\>	Mean size of crystallites (nm)
P1	$\varepsilon = 0\%$	0.0422	13.8	0.0417	14.0
	$\varepsilon = 50\%$	0.0461	12.7	0.0489	11.9
	$\varepsilon = 100\%$	0.0517	11.3	0.0554	10.5
	Release	0.0502	11.6	0.0525	11.1
P3	$\varepsilon = 0\%$	0.0497	11.8	0.0494	11.8
	$\varepsilon = 50\%$	0.0527	11.1	0.0526	11.1
	$\varepsilon = 100\%$	0.0503	11.6	0.0524	11.2
	Release	0.0493	11.8	0.0491	11.9

Extended Data Figure 4 | Thin-film characterization of damaged and healed P3 and P5. a, **b**, Atomic force microscopy images of damaged (**a**) and healed (**b**) thin film of **P3** after solvent and thermal annealing. We note that all the previously observed nanocracks were absent after the healing process. **c**, Dichroic ratio of **P3** healed thin film as determined by polarized ultraviolet–visible spectroscopy. **d**, **e**, Atomic force microscopy images of damaged (**d**) and healed (**e**) thin film of **P5** after solvent and thermal annealing. We observed that a small number of nanocracks

remained in the film. **f**, Dichroic ratio of **P5** healed thin film as determined by polarized ultraviolet–visible spectroscopy. We observed that the dichroic ratio of healed film of **P3** fully recovered to a value similar to that of the pristine film without damage. On the other hand, when **P5** is subjected to the same treatment, the dichroic ratio was not restored, indicating that the movement of the polymer chains was insufficient to restore the film's mechanical properties.

a

Transferred CNT electrode (Gate)

SEBS (Substrate)

Gate

Transferred PDMS (Dielectric)

SEBS (Substrate)

Dielectric

Spray-coated CNT/PEDOT:PSS electrode (S&D)

CNT

PEDOT:PSS

DPP-based polymer

Stretchable Dielectric

CNT (Gate)

SEBS (Substrate)

Source & Drain

Transferred DPP-based Polymer

Stretchable Dielectric

SEBS (Substrate)

Semi-conductor

b

c

Extended Data Figure 5 | Fabrication and electronic properties of a fully stretchable 5 × 5 transistor array. a, Fabrication process of fully stretchable OTFTs. (1) Transfer printing of the carbon nanotube gate electrode as prepared by spray-coating a carbon nanotube solution (10 mg ml^{-1} in CHCl$_3$) on SEBS substrate (thickness 200 μm). (2) Contact transfer printing of PDMS dielectric layer as prepared by spin-coating a diluted PDMS (220 mg ml^{-1} in CHCl$_3$) on OTS-treated SiO$_2$ substrate on a carbon nanotube gate electrode. (3) Contact transfer printing of semiconducting polymer layer (prepared by spin coating onto OTS-treated SiO$_2$ substrate) on PDMS dielectric layer. (4) Spray coating of carbon nanotube (70 nm)/PEDOT:PSS (30 nm) source and drain electrodes on the semiconducting layer. **b**, **c**, On/off current mapping (**b**) and statistical distribution (**c**) of 5 × 5 fully stretchable OTFT arrays (width 1,000 μm; length 150 μm). Number of devices from a single substrate, $n = 25$.